



Article

Improved Polar Current Shell Algorithm for Ocean Current Retrieval from X-Band Radar Data

Yi Li, Zhiding Yang and Weimin Huang *

Department of Electrical and Computer Engineering, Memorial University of Newfoundland, St. John's, NL A1B 3X5, Canada; yli22@mun.ca (Y.L.); zhidingy@mun.ca (Z.Y.)

* Correspondence: weimin@mun.ca

Abstract: This paper presents an improved algorithm for retrieving ocean surface currents from X-band marine radar images. The original polar current shell (PCS) method begins with a 3D fast Fourier transform (FFT) of the radar image sequence, followed by the extraction of the dispersion shell from the 3D image spectrum, which is then transformed into a PCS using polar coordinates. Building on this foundation, the improved approach is to analyze all data points corresponding to different wavenumber magnitudes in the PCS domain rather than analyzing each specific wavenumber magnitude separately. In addition, kernel density estimation (KDE) to identify high-density directions, interquartile range filtering to remove outliers, and symmetry-based filtering to further reduce noise by comparing data from opposite directions are also utilized for further improvement. Finally, a single curve fitting is applied to the filtered data rather than conducting multiple curve fittings as in the original method. The algorithm is validated using simulated data and real radar data from both the Decca radar, established in 2008, and the Koden radar, established in 2017. For the 2008 Decca radar data, the improved PCS method reduced the root-mean-square deviation (RMSD) for speed estimation by 0.06 m/s and for direction estimation by 3.8° while improving the correlation coefficients (CCs) for current speed by 0.06 and direction by 0.07 compared to the original PCS method. For the 2017 Koden radar data, the improved PCS method reduced the RMSD for speed by 0.02 m/s and for direction by 4.6°, with CCs being improved for current speed by 0.03 and direction by 0.05 compared to the original PCS method.

Keywords: ocean current measurement; PCS algorithm; X-band marine radar; signal processing



Citation: Li, Y.; Yang, Z.; Huang, W. Improved Polar Current Shell Algorithm for Ocean Current Retrieval from X-Band Radar Data. *Remote Sens.* **2024**, *16*, 4140. <https://doi.org/10.3390/rs16224140>

Academic Editor: Kaoru Ichikawa

Received: 21 September 2024

Revised: 4 November 2024

Accepted: 5 November 2024

Published: 6 November 2024



Copyright: © 2024 by the authors. Licensee MDPI, Basel, Switzerland. This article is an open access article distributed under the terms and conditions of the Creative Commons Attribution (CC BY) license (<https://creativecommons.org/licenses/by/4.0/>).

1. Introduction

The retrieval of ocean surface currents plays a crucial role in a variety of marine applications, including navigation, coastal monitoring, Search-and-Rescue (SR) missions, oil spill response, and marine debris tracking [1,2]. Traditional methods for measuring ocean surface currents, such as drifting buoys [3,4], acoustic doppler current profilers (ADCPs) [5,6], and current meters [7], although useful for providing localized current data, have significant limitations. These methods are often costly to deploy, complex to maintain, limited in spatial coverage, and challenging to operate continuously in harsh marine environments. The data they collect are typically point-based, which fail to capture the broader dynamics of ocean currents over large areas [8]. With advancements in technology, remote sensing offers the capability to provide large-scale, real-time, and continuous surface current data, allowing researchers to gather comprehensive flow information without direct contact with the ocean [9]. This significantly enhances the efficiency and spatial coverage of data acquisition [10]. Several types of sensors, such as high-frequency (HF) radars [11–13], X-band marine radars [14], satellite altimeters [15], and synthetic aperture radars (SAR) [16], have commonly been used in remote sensing to measure ocean surface currents in recent years. Compared to other remote sensing sensors, X-band radars hold significant advantages when monitoring ocean surfaces within a range of several

kilometres [17]. Their high spatial and temporal resolution allows for the precise tracking of small-scale current [18], wind [19,20], and wave dynamics [21–24]. The ease of deployment, lower maintenance requirements, and cost-effectiveness of X-band radars further enhance their practicality for ocean surface measurements [25].

When an X-band radar transmits electromagnetic waves, they interact with the ocean surface waves that match the Bragg scattering condition, where the radar wavelength is twice that of the ocean waves. This scattering mechanism amplifies the backscatter signal, which can provide detailed information about the sea surface. It is found that the motion of the surface waves influenced by currents will cause an extra Doppler shift in the frequency of the backscattered signals [9]. Based on this principle, several algorithms have been developed for retrieving ocean currents from X-band radar data. Traditional approaches include the least-squares (LS) curve-fitting technique [9], the iterative LS (ILS) approach [26], the weighted least-squares (WLS) method [27], the dispersive surface classifier (DiSC) method [28], and the normalized scalar product (NSP) procedure [14]. A more recent development is the polar current shell (PCS) method [29], which transforms radar image spectra into polar coordinates for surface current retrieval. This method offers a robust alternative to previous approaches by providing a more structured framework for current estimation. Dual-polarized radar systems have also been shown to improve current retrieval accuracy, with certain sea state conditions benefiting from vertical polarization [30]. Chen et al. [31] demonstrated an improved cross-spectral correlation approach for deriving sea surface currents from X-band marine radar images, providing another robust method comparable to traditional fast Fourier transform (FFT)-based methods. In a recent study by Wu et al. [32], the local phase gradient-based method is employed to effectively estimate spatial currents despite the complex circulation patterns inherent to bay areas. Moreover, Wang et al. [33] demonstrated the application of machine learning algorithms, including linear regression and neural networks, to enhance the estimation of surface current from radar data. With the maturation of technology, X-band marine radars have also developed several commercial applications for current measurements, such as WaMos II [34]. This system provides real-time, high-resolution current data under various weather conditions and is widely used in marine engineering. For instance, Derkani et al. [35] utilized WaMoS II during the Antarctic Circumnavigation Expedition to collect wave spectra and surface current data, applying calibration methods to improve data accuracy and validating the results with satellite observations.

Despite these advancements, challenges remain in current retrieval, especially when dealing with noisy datasets or outliers that can degrade the accuracy of the results. In low-sea-state conditions, traditional radar methods (e.g., ILS and NSP) struggle due to the lower signal-to-noise ratios of radar backscatter from calm sea surfaces, as noted by Huang et al. [36]. The original PCS method, while robust in many scenarios, can produce inaccurate results when the number of valid data points for curve fitting is insufficient or when noise is prevalent. Moreover, inaccurate current estimation may affect subsequent wave parameter estimations [37,38]. This limitation underscores the necessity for an improved PCS algorithm that addresses these issues. In response, this paper introduces an improved PCS algorithm with several key enhancements. The improved algorithm incorporates an outlier rejection process to filter noise before curve fitting, as well as a unified fitting method that considers the entire dataset collectively, reducing localized errors. Symmetry-based noise filtering is also introduced according to the symmetry of Doppler-shifted dispersion shells, further refining the results. These improvements have been validated using both simulated and real radar data, showing significant gains in accuracy without adding to the computational complexity.

The structure of this paper is as follows: Section 2 details the original PCS method, followed by Section 3, which presents the specific improvements made to the PCS algorithm. Section 4 provides performance validation through simulations, while Section 5 applies the improved method to real-world radar data. Finally, Section 6 concludes with recommendations for further research and potential future improvements.

2. The PCS Current Algorithm

The PCS algorithm [29] provides an efficient approach for estimating ocean surface currents using X-band marine radar data by transforming radar image spectra into polar coordinates. The detailed current retrieval processes are described as follows.

2.1. Image Spectrum Generation

The process starts by selecting a sequence of sub-regions ($I \in \mathbb{R}^{x \times y \times t}$) from the original radar images, where $x \times y$ defines the spatial dimensions of each sub-image, and t is the number of images in the sequence, representing the temporal dimension. In this work, x , y , and t are equal to 128, 128, and 32. To enhance contrast and minimize background noise, the mean intensity of each sub-region is subtracted from the pixel values. Next, to reduce the Gibbs phenomenon, a tapering function is applied. The frequency resolution is then improved by applying zero-padding, expanding the data dimensions to $256 \times 256 \times 256$. This zero-padding size was chosen based on balancing the computational load spectral resolution. The power spectrum, $P_0(k_x, k_y, \omega)$, is finally derived by squaring the spectral amplitude obtained from the three-dimensional (3D) FFT.

2.2. Dispersion Shell Identification

The dispersion shell is identified based on the linear (fundamental) wave dispersion relationship, assuming deep water conditions. The dispersion relation, including the effect of ocean currents, is given by

$$\omega = \sqrt{gk} + \vec{k} \cdot \vec{U} \quad (1)$$

where ω is the angular frequency, which includes the Doppler shift from the current, g is the gravitational acceleration, $k = \sqrt{k_x^2 + k_y^2}$ is the wavenumber magnitude, \vec{U} is the surface current velocity vector, and $\vec{k} \cdot \vec{U} = kU \cos(\theta)$ is the Doppler shift caused by the ocean current, with θ being the angle between the current direction and the wave vector direction.

For each wavenumber vector (k_x, k_y) in the wavenumber plane, a series of angular frequencies $(\omega_1, \omega_2, \dots, \omega_{128})$ is associated. If the maximum energy within this set is lower than a predefined threshold, P , the corresponding set $(\omega_1, \omega_2, \dots, \omega_{128})$ is discarded. For wavenumber vectors where the maximum energy exceeds the threshold, P , only one specific triplet (k_x, k_y, ω_i) corresponds to the ocean wave component that lies on the dispersion shell. This angular frequency, ω_i , is identified by detecting the most prominent energy peak in the series of frequencies for each wavevector. This procedure is applied to all wavenumber vectors (k_x, k_y) , ultimately extracting the dispersion shell, $\omega(k_x, k_y)$.

2.3. Conversion to Polar Coordinates

Based on the fundamental relation, the frequency shift caused by the surface current is given by

$$\omega_U = \vec{k} \cdot \vec{U} = kU \cos(\theta) \quad (2)$$

where ω_U is the Doppler-shifted angular frequency due to the current, k is the wavenumber magnitude, U is the magnitude of the surface current speed, and θ is the angle between the wave vector and the current direction.

Next, the Cartesian current shell, $\omega_U(k_x, k_y)$, is transformed into polar coordinates to form the polar current shell, denoted as $\omega_U(k, \theta_k)$, where $k = \sqrt{k_x^2 + k_y^2}$ is the radial wavenumber, and θ_k represents the direction of the wave vector in polar coordinates. This transformation allows for easier analysis of the surface current effects by examining the data along specific radii and angular directions.

2.4. Current Estimation Through Curve Fitting

To estimate the surface current, Grubbs' test [39] is applied to remove outliers along each radial direction. After eliminating the outliers, least-squares curve fitting is performed along the circumferential direction for each fixed radial wavenumber k . The fitting uses a sinusoidal model to determine the current speed, U , and direction, ϕ_U , minimizing the error cost function. The model function for curve fitting is given by

$$f(U, \bar{\theta}) = \frac{\omega_U}{k} = U \cos \bar{\theta} = U \cos(\theta_k - \phi_U) \quad (3)$$

The error cost function, which is minimized during the fitting process, is expressed as

$$E = \sum_{d=1}^{N_d} \left[\frac{\omega_{U_d}}{k} - U \cos(\theta_{k_d} - \phi_U) \right]^2 \quad (4)$$

where N_d is the number of points on the shell extracted in the circumferential direction for a specific k , θ_{k_d} is the wavevector direction, and ϕ_U is the surface current direction.

If the number of extracted shell points, N_d , for a specific wavenumber k is less than 10, the curve-fitting process for that k is terminated, and no results are retrieved for that wavenumber. The angle corresponding to the maximum value of the estimated function, $f(U, \bar{\theta})$, is taken as the current direction, and the amplitude of the sinusoidal function represents the current speed. Finally, by averaging the results across different wavenumber magnitudes, a robust estimate of the current parameters is obtained.

2.5. Limitation Analysis

Based on our experiment, it was found that the original PCS method has some limitations. First, while Grubbs' test is used to detect outliers, not all instances of noise or aliasing appear as clear outliers. Second, curve fitting in the original method for a specific wavenumber k will be terminated if the number of data points available is less than 10, leading to a loss of potentially valuable data. This is not favorable, especially for sparse datasets. Since no fitting results are generated for these k -values, the accuracy of the method may be reduced. Moreover, if a specific k -value is strongly affected by noise, the fit result may be significantly biased. Then, during the final averaging step, these biased results can significantly affect the overall estimation, leading to a deviation from the true current parameters.

3. Improved PCS Method

Considering the potential issues with the original method, the improved PCS method incorporates several enhancements to increase the algorithm's accuracy and robustness. The original PCS method also has certain limitations, as discussed in Section 4. It is worth noting that the improved method performs an analysis for all wavenumber magnitudes within the polar current shell rather than conducting filtering and curve fitting for each wavenumber magnitude separately. The key improvements include better noise filtering, outlier rejection, and single curve fitting. These advancements address limitations in the original method, improving the precision of ocean current estimation.

3.1. Kernel Density Estimation-Based Direction Filtering

The kernel density estimation (KDE) technique [40] is applied to estimate the density of the initial unfiltered data (\mathbf{z}_i) across all values of k in a specific direction, $i, i = 1, 2, 3, \dots, 360$. As for the observed data points \mathbf{z}_i in the i th direction, the estimated density, $\hat{f}_i(x)$, at a any point x within the domain of input data can be expressed as

$$\hat{f}_i(x) = \frac{1}{nh} \sum_{s=1}^{N_s} K\left(\frac{x - z_{i_s}}{h}\right) \quad (5)$$

where z_{i_s} is the s th data point in \mathbf{z}_i , $\mathbf{z}_i = [z_{i_1}, z_{i_2}, \dots, z_{i_{N_s}}]$, N_s is the number of points in \mathbf{z}_i , h is the bandwidth parameter obtained by Silverman's rule [41], which can control the smoothness of the density estimate, and K is the Gaussian kernel function in this study. After calculating the density in each direction, data points, denoted as \mathbf{z}'_i , within the range where the density in each direction exceeds half of the maximum density ($\hat{f}_i^{\max}(x) = \max(\hat{f}_i(x))$) are retained for further processing. Thus, the filtered data in all directions can be expressed as

$$\mathbf{Z}' = [\mathbf{z}'_1; \mathbf{z}'_2; \mathbf{z}'_3; \dots; \mathbf{z}'_{360}], \quad (6)$$

and the mean max density in all directions can be given by

$$\bar{f}^{\max}(x) = \frac{\sum_{i=1}^{360} (\hat{f}_i^{\max}(x))}{360} \quad (7)$$

Then, those directions in $\hat{f}_i^{\max}(x)$ where the corresponding density value exceeds 60% of $\bar{f}^{\max}(x)$ are identified, and all data along these selected directions are extracted from \mathbf{Z}' . The selected data can be denoted as \mathbf{Z}'_{f_1} and utilized and analyzed for the following steps.

This filtering step significantly reduces the influence of outliers and noise before the next filtering stage. By focusing on high-density regions, the algorithm ensures that the most reliable data are retained, improving the overall accuracy of current estimation.

3.2. Interquartile Range Noise Filtering

Once the high-density directions are identified from the filtered dataset, \mathbf{Z}'_{f_1} , obtained from the KDE process, interquartile range (IQR) filtering [42] is applied as the next step to further refine the dataset. This filtering technique is used to remove outliers from the data in each direction, ensuring that the data better represent the underlying distribution.

For each direction, the interquartile range is calculated as

$$IQR = Q_3 - Q_1 \quad (8)$$

where Q_1 is the 25th percentile (lower quartile) and Q_3 is the 75th percentile (upper quartile) of the data points \mathbf{Z}'_{f_1} . Data points are considered outliers if they fall below the lower bound or above the upper bound, defined as

$$\text{Lower bound} = Q_1 - 1.5 \times IQR \quad (9)$$

$$\text{Upper bound} = Q_3 + 1.5 \times IQR \quad (10)$$

Any data points \mathbf{Z}'_i from \mathbf{Z}'_{f_1} that fall outside the range [Lower bound, Upper bound] are considered noise or outliers and are removed. The resulting filtered dataset after applying IQR filtering is denoted as \mathbf{Z}'_{f_2} .

This step ensures that outliers within the high-density regions are removed, further refining the dataset. Since the noise is significantly reduced, the filtered result \mathbf{Z}'_{f_2} can improve the accuracy of subsequent curve fitting.

3.3. Symmetry-Based Opposite-Direction Noise Reduction

After the interquartile range (IQR) filtering in step 3.2, which identified and removed outliers from the dataset \mathbf{Z}'_{f_1} , symmetry-based opposite-direction noise reduction is applied. This step aims to reuse data points that may have been filtered out in the previous steps but are deemed reliable due to their symmetric counterparts in the data. At the same time, it also filters out data that do not satisfy the symmetry conditions, further refining the dataset.

The symmetry principle dictates that wavevectors that are symmetric around the origin should experience Doppler shifts of equal magnitude but with opposite signs [43]. For each pair of wavevectors $\vec{k}(k_x, k_y)$, its symmetric counterpart can be expressed as

$\vec{k}'(-k_x, -k_y)$. According to Equation (2), the Doppler shift of the symmetric counterpart $\vec{k}'(-k_x, -k_y)$ becomes

$$\omega'_u = -kU \cos(\theta) \tag{11}$$

In an ideal, noise-free scenario, the sum of the Doppler shifts for symmetric wavevectors should be zero, i.e.,

$$\omega_u + \omega'_u = 0 \tag{12}$$

Figure 1 shows an example of the (a) intrinsic and (b) Doppler-shifted dispersion shells in the (k_x, k_y, ω) domain. A and B are two spectral points for two wavevectors symmetric about the origin of the wavenumber plane. In Figure 1a, their angular frequencies are shown to be the same, which are both ω_0 . In Figure 1b, the Doppler shift of A is ω_{uA} , and the Doppler shift of B is ω_{uB} . In addition, the sum of ω_{uA} and ω_{uB} should be zero under ideal conditions.

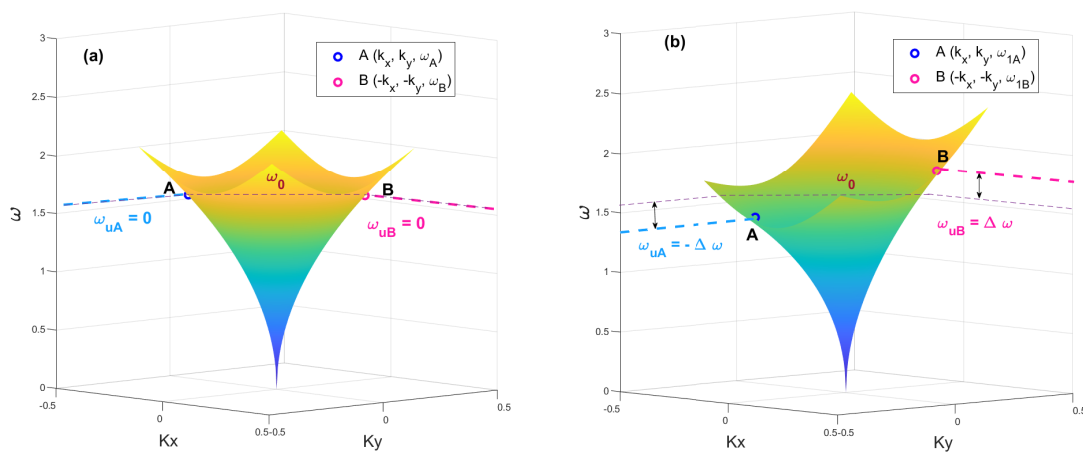


Figure 1. An example of the (a) intrinsic and (b) Doppler-shifted dispersion shells in the (k_x, k_y, ω) domain. Different colors represent the different ω values.

In addition, Doppler shifts per unit wavenumber can be expressed by dividing both terms by k :

$$\frac{\omega_u}{k} + \frac{\omega'_u}{k} = 0 \tag{13}$$

In this step, the algorithm calculates the difference in Doppler shifts per unit wavenumber between each pair of symmetric wavevectors:

$$S_\omega(\vec{k}, \vec{k}') = \left| \frac{\omega_u}{k} + \frac{\omega'_u}{k} \right| \tag{14}$$

If the calculated difference, $S_\omega(\vec{k}, \vec{k}')$, is below a predefined threshold, the data point is retained. Specifically, the range of k values filtered out in Section 3.2 is within the bounds of [Lower bound, Upper bound]. Therefore, for the wavevector \vec{k}' symmetric to \vec{k} , the threshold for k' is set within the bounds of $[-\text{Upper bound}, -\text{Lower bound}]$. This ensures that the symmetry between \vec{k} and \vec{k}' is maintained, and that only data points satisfying this condition are retained for further analysis.

This step ensures that any data points conforming to the symmetry principle are retained, while noise and inconsistencies are further filtered out. The final filtered dataset after applying this symmetry-based noise reduction is denoted as Z'_{f3} . This refined dataset provides a more reliable basis for subsequent curve fitting.

3.4. Unified Curve Fitting for Filtered Data

After the data have been filtered, the improved PCS method applies a unified curve-fitting process to all the filtered data points, k_1, k_2, \dots, k_m , which is the same as the curve-fitting process explained in Section 2.4. Unlike the original PCS method, where curve fitting was performed separately for different radii k , the improved method fits a single sinusoidal curve to the entire filtered dataset, Z'_{f3} . This approach minimizes the potential for localized fitting errors and ensures that the final current speed and direction estimates are more consistent and accurate across the entire wave spectrum. Unified fitting also helps to reduce the impact of aliasing by incorporating a broader range of reliable data into the curve-fitting process.

4. Experiments and Results

4.1. Experiment on Simulated Data

In this section, experiments were conducted using radar data simulated under two different antenna rotation speeds (RPM: 24 and 48). The simulated radar data are generated using a modified Pierson–Moskowitz (P-M) wave spectrum [44] integrated with a cardioid directional spreading function [45]. The PM spectrum models a fully developed sea, and it has been widely used [46,47].

To simulate ocean current effects, additional parameters were introduced into the dataset to include surface currents with specific speeds and directions. The simulated dataset includes two files: one corresponding to an antenna rotation speed of 24 RPM, along with a current speed range between 0.5 and 10 m/s with a current direction of 150° , and another file with a 48 RPM rotation speed, covering a current speed range from 0.5 to 15 m/s and a current direction of 180° . Since the experiment considers simulations of radar measurements under different vessel speeds, the range of input current speeds in this experiment is larger than that of the usual current speed. These files were processed using three different methods, PCS, improved PCS, and NSP, to evaluate each method's performance under different sea state conditions.

4.1.1. Limitation Analysis and Improvement

To analyze the limitations of the original PCS method and demonstrate the improvements introduced by the improved PCS method, one radar image file from the 24 RPM simulated data series, as shown in Figures 2 and 3, is selected as an example. The current speed in this simulation is 7.5 m/s, and the current direction is 150° .

(a) Analysis of Original PCS Results

Figure 2a shows all the data after being converted to the PCS domain, plotted against different k values. This represents the raw data before any outlier removal or filtering is applied. The spread of data points indicates significant noise and aliasing, especially at higher k values. Figure 2b presents the data after applying the original PCS method's outlier removal process. Here, some of the noise has been removed by the original PCS method, but outliers are still present, particularly in regions with higher variability, suggesting that the original outlier removal process is not fully effective. Figure 2c shows the curve-fitting results for different k vectors after applying the original PCS method. The curve fitting is highly impacted by the remaining outliers and noise, leading to significant deviations in current speed and direction estimations. Although averaging all the fitted results can improve the results a little bit, the overall poor fit highlights the limitations of the original PCS method in handling low-RPM scenarios and noisy data.

(b) Analysis of Improved PCS Results

Figure 3a shows all the data after being converted to the PCS domain, similar to Figure 2a. This serves as the starting point before applying any filtering or noise reduction techniques in the improved PCS method. The data still exhibit significant noise and variability, particularly at higher k values. Figure 3b presents the data after applying

KDE-based direction filtering. KDE helps to highlight the most probable directions by reducing the influence of extreme outliers, resulting in a more concentrated and reliable data distribution compared to the unfiltered data in Figure 3a. Figure 3c shows the data after applying interquartile range (IQR) noise filtering. The IQR filtering process further refines the data by removing points that fall outside the interquartile range, which are likely to be noise or outliers. The data appear more consistent and aligned, indicating a significant reduction in noise. Figure 3d shows the data after restoring certain points filtered out by the IQR method. Specifically, points that had been removed due to their low density but satisfy the symmetry with high-density directional values are recovered. This results in a dataset that is both clean and retains important symmetric information, making it more comprehensive than the one shown in Figure 3c.

Finally, Figure 3e presents the unified curve fitting for the filtered data. After applying all the filtering techniques, the final curve-fitting process is applied, resulting in a smooth, well-fitted curve that accurately represents the current speed and direction. The improved PCS method's curve fitting is much more precise compared to the original method, as shown by the reduced deviation and noise.

The improved PCS method significantly reduces the influence of outliers and noise, as evidenced by the tighter clustering of data points and the smoother curve fitting observed in the final result. The aliasing effects seen in the original method have also been largely mitigated, providing a more accurate representation of the current speed and direction.

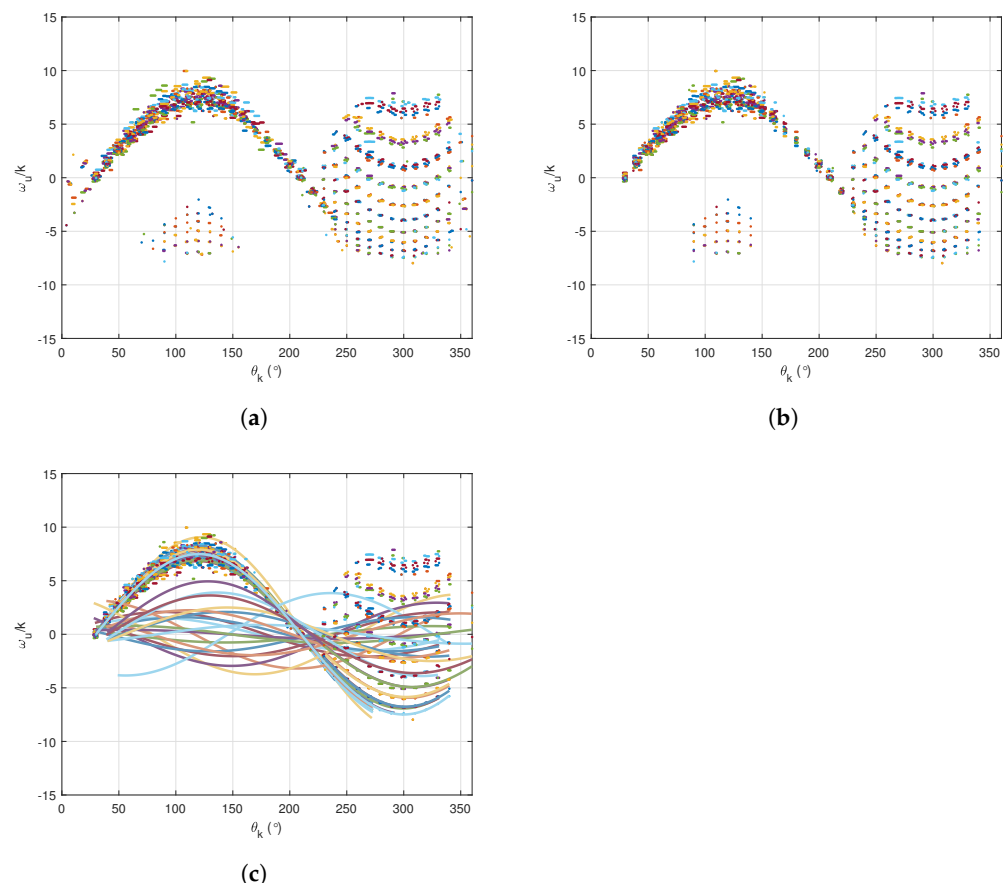


Figure 2. (a) Description of all the data after converting to the polar current shell (PCS) domain. (b) Description of the data after applying the original PCS method's outlier removal process. (c) Description of the curve-fitting results for different k vectors. Different colors correspond to different values of wavenumber k .

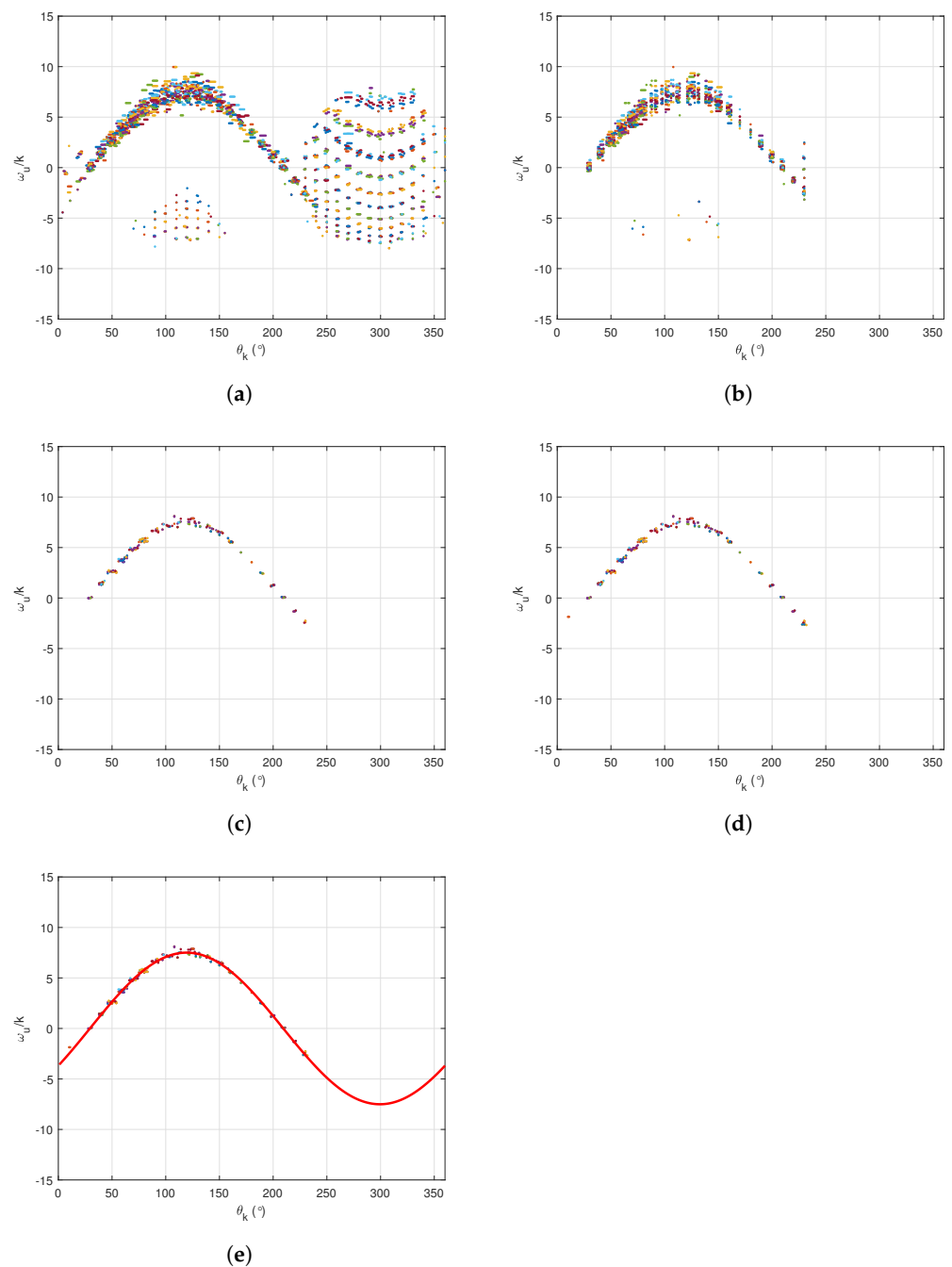


Figure 3. Description of (a) all the data after converting to the PCS domain, (b) kernel density estimation (KDE)-based direction-filtering result, (c) interquartile range noise filtering result, (d) symmetry-based opposite direction noise reduction result, and (e) unified curve fitting for filtered data.

4.1.2. Analysis of the Results

The results are shown in Figure 4 and Table 1, which illustrate the performance of the original and improved PCS methods under two different RPM conditions (24 and 48 RPM).

In Figure 4, different methods are represented by distinct markers: a blue * indicates the results of the NSP method, a black x represents the results of the original PCS method, and red circles stand for the results of the improved PCS method. The solid line represents the true values. The graphs depict the retrieved current speed and direction against the input speed for two different rotation speeds, 24 RPM and 48 RPM. Table 1 presents the error analysis of the simulated data, including the correlation coefficient (CC) and RMSD for speed and direction estimates. It shows the performance of each method in terms

of speed and direction accuracy across different RPM values. A noticeable observation from Figure 4 and Table 1 is that the original PCS method exhibits significant errors at 24 RPM, particularly in current speed estimation. The improved PCS method, in contrast, consistently delivers better accuracy, as reflected in the smaller RMSD values and higher correlation with the true values.

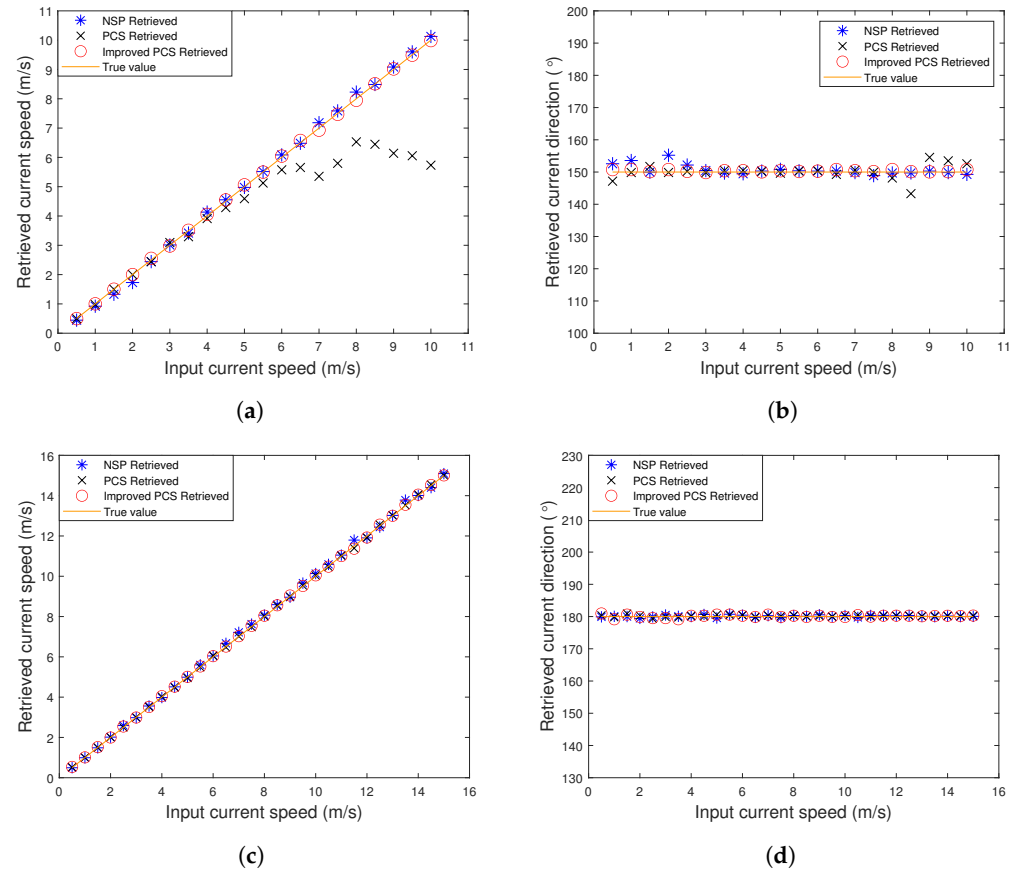


Figure 4. (a) Retrieved current speed versus input speed at revolutions per minute (RPM) = 24. (b) Retrieved current direction versus input speed at RPM = 24. (c) Retrieved current speed versus input speed at RPM = 48. (d) Retrieved current direction versus input speed at RPM = 48.

Table 1. Error analysis of simulated data.

File	RPM	Method	CC		RMSD		Current Speed Range [m/s]	Current Direction [°]
			Speed	Direction	Speed [m/s]	Direction [°]		
1	24	PCS	0.93	1	0.86	2.8	0.5–10	150
		Improved PCS	1	1	0.07	0.8		
		NSP	0.96	1	0.09	0.9		
2	48	PCS	1	1	0.06	0.7	0.5–15	180
		Improved PCS	1	1	0.04	0.4		
		NSP	1	1	0.08	1.1		

(a) Estimated Result Comparison at 24 RPM

At 24 RPM, as shown in Figure 4a,b, the original PCS method suffers from noticeable deviations in both speed and direction estimates. Specifically, the speed estimate tends to diverge significantly as the input speed increases beyond 5 m/s, as illustrated by the blue x in Figure 4a. The improved PCS method, represented by red circles, significantly reduces these deviations, providing results much closer to the true values (the solid line).

This is further confirmed in Table 1, where the speed RMSD of the improved PCS method is 0.07 m/s and 0.86 m/s for the original PCS.

For current direction, as shown in Figure 4b, the original PCS method still maintains relatively consistent direction estimates, but deviations become more pronounced at higher input speeds. The improved PCS method also performs better than the original, with an RMSD of 0.8° compared to 2.8° for the original PCS. The green x representing the NSP method also provides more accurate estimates than the original PCS but is less accurate than the improved PCS method.

The increased error in the original PCS method at 24 RPM can be attributed to the lower temporal resolution associated with the slower antenna rotation speed. At 24 RPM, fewer radar sweeps are performed per second, which reduces the temporal frequency of the data collection. This limitation particularly affects high-speed currents, where rapid changes in current speed and direction are harder to capture with fewer data points. As the input current speed increases beyond 5 m/s, the original PCS method struggles to accurately track these rapid variations, leading to significant deviations in both speed and direction estimates.

(b) Estimated Result Comparison at 48 RPM

At 48 RPM, the performance of the original PCS method improves, as depicted in Figure 4c,d. The speed and direction estimates become more reliable compared to the results at 24 RPM, with an RMSD of 0.06 m/s for speed and 0.7° for direction. However, the improved PCS method still shows less error, with an RMSD of 0.04 m/s for speed and 0.4° for direction, as shown in Table 1. The green x representing the NSP method also provides reasonable accuracy but remains less effective than the improved PCS method.

Overall, the improved PCS method consistently outperforms both the original PCS and NSP methods, particularly at lower RPMs. The improved PCS method demonstrates higher accuracy in both speed and direction estimates, with significantly lower RMSD values across different conditions. These results suggest that the improved PCS method is more robust and reliable for retrieving ocean currents from X-band radar data, especially in low-RPM scenarios.

4.2. Experiment on Real Data

This section provides an overview of the real-world validation performed using radar data from various sea trials.

4.2.1. Analysis of Decca Radar Data

(a) Data Description

The first dataset analyzed in this study was provided by Defence Research and Development Canada (DRDC) and collected during a sea trial from 25 November to 4 December 2008, approximately 220 km off the coast of Halifax. The experiment utilized HH-polarized shipborne Decca marine radars, operating at a frequency of 9.41 GHz and covering a full 360° azimuth. For the purpose of this study, the radar data had a maximum range of 2160 m and a resolution of 7.5 m. Excluding the completely black images with no wave signature caused by system errors, a total of 2041 radar images were analyzed. The radar signals were processed using the Wave Monitoring System II (WaMoS II), which digitized them into 8-bit image intensities. The surface current data obtained from the WaMoS II system serve as a reference for validating the accuracy of our algorithm in estimating ocean surface currents.

(b) Comparison of Encounter Current Velocity Estimation

Since the radar data were collected from a moving ship in this study, the encounter current is analyzed first. Encounter current refers to the relative current experienced by the moving ship, as it moves through the sea. This is the combined effect of the actual surface current and the movement of the ship itself. The comparison of the encounter current

estimation results between the improved PCS, PCS, and NSP methods is shown in Figure 5. The range of -40° to 400° in Figure 5b is set to avoid oscillations or abrupt changes in the estimated direction near the 0° and 360° boundaries. Directional data often wrap around at 0° or 360° , which can cause sudden jumps or oscillations when visualized. By extending the range beyond the typical $0\text{--}360^\circ$ range, this issue is mitigated, allowing for a smoother representation of the directional estimates.

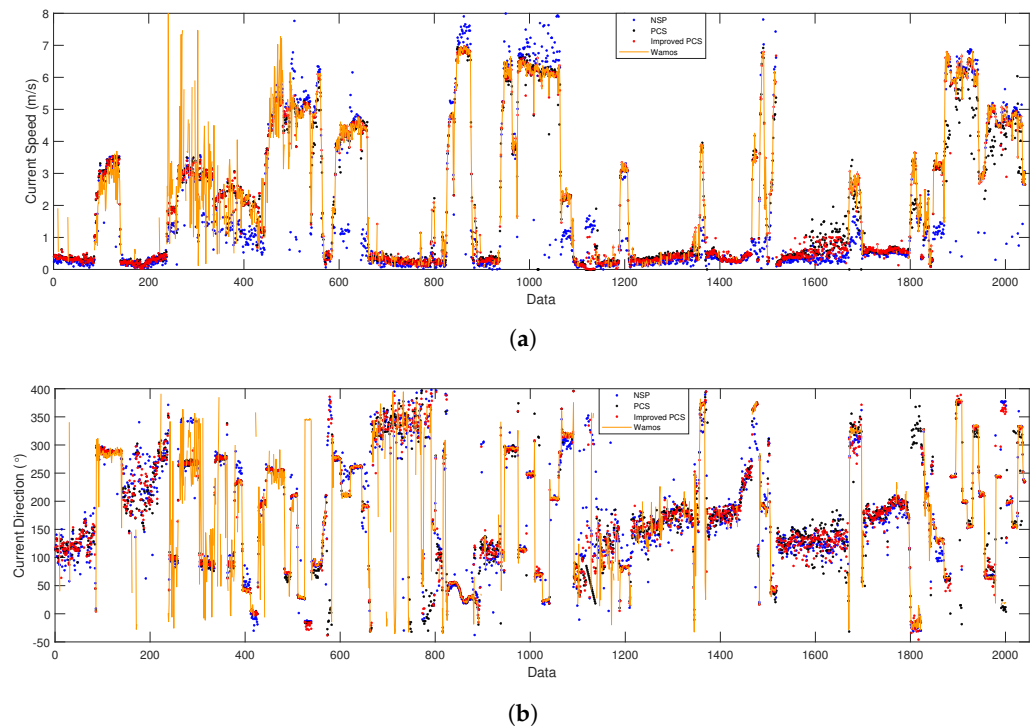


Figure 5. (a) Comparison of encounter current speed and (b) encounter current direction obtained from Decca radar data.

According to Table 2, the CC between the speed estimates from the improved PCS method and the reference WaMos data is 0.99, which is higher than that (0.92) of the original PCS method and that (0.91) of the NSP method. The improved PCS algorithm has an RMSD of 0.38 m/s, whereas the original PCS and NSP methods show higher RMSD values of 0.51 m/s and 1.14 m/s, respectively. The improved PCS estimates are closely aligned with the reference WaMos data, while the original PCS and NSP methods show higher deviations, particularly in areas with significant speed changes. Higher CC and lower RMSD values were obtained for the improved PCS method.

Table 2. Error analysis of encounter current estimation based on 2008 radar data.

Method	CC		RMSD	
	Speed	Direction	Speed [m/s]	Direction [°]
Improved PCS	0.99	0.93	0.38	20.3
PCS	0.92	0.90	0.51	24.6
NSP	0.91	0.91	1.14	25.2

The improved PCS method has a CC of 0.93 for current direction and is superior to the PCS (0.90) and NSP (0.91) methods. For RMSD, the improved PCS algorithm has the lowest error of 20.3° , compared to 24.6° for PCS and 25.2° for NSP. Figure 5b demonstrates that the original PCS method shows some deviation in sections with directional shifts. In contrast, the improved PCS method aligns with the WaMos reference.

(c) Motion Compensation

To accurately estimate the surface current from the radar data, it is essential to account for the ship's motion by subtracting the ship's speed from the encounter current (U_{en}). However, as noted by Bell et al. [48], inconsistencies in the ship's speed within certain radar image sequences can create difficulties in determining the true ship speed. Figure 6 shows an example of these inconsistencies in ship speed data recorded during the radar data collection process.

```

CC      ***** START FRAMEDATA SECTION *****
CC      Date      Time      GYROC  SHIPS  RPT
F0001  11-28-2008  20:47:14.531  96.5   11.8   2.063
F0002  11-28-2008  20:47:16.640  97.0   11.7   2.095
F0003  11-28-2008  20:47:18.734  97.6   11.3   2.108
F0004  11-28-2008  20:47:20.812  97.3   11.9   2.080
F0005  11-28-2008  20:47:22.875  96.9   11.9   2.072
F0006  11-28-2008  20:47:24.968  96.6   11.4   2.075
F0007  11-28-2008  20:47:27.046  96.9   11.5   2.090
F0008  11-28-2008  20:47:29.125  97.7   11.4   2.081
F0009  11-28-2008  20:47:31.203  97.2   11.4   2.075
F0010  11-28-2008  20:47:33.281  97.4   11.7   2.077
F0011  11-28-2008  20:47:35.375  97.7   11.4   2.089
F0012  11-28-2008  20:47:37.453  97.4   11.4   2.088
F0013  11-28-2008  20:47:39.531  97.1   11.4   2.071
F0014  11-28-2008  20:47:41.625  97.4   11.4   2.156
F0015  11-28-2008  20:47:43.703  97.4   11.4   2.084
F0016  11-28-2008  20:47:45.796  97.1   11.4   2.080
F0017  11-28-2008  20:47:47.875  96.8   11.4   2.083
F0018  11-28-2008  20:47:49.953  96.5   11.3   2.082
F0019  11-28-2008  20:47:52.046  96.9   11.3   2.093
F0020  11-28-2008  20:47:54.125  97.1   11.3   2.080
F0021  11-28-2008  20:47:56.187  96.6   11.3   2.066
F0022  11-28-2008  20:47:58.281  97.0   11.2   2.084
F0023  11-28-2008  20:48:00.359  97.3   10.5   2.086
F0024  11-28-2008  20:48:02.421  96.8   10.9   2.062
F0025  11-28-2008  20:48:04.500  97.1   10.3   2.071
F0026  11-28-2008  20:48:06.578  97.6   10.3   2.084
F0027  11-28-2008  20:48:08.640  97.6   10.6   2.066
F0028  11-28-2008  20:48:10.703  97.0   10.5   2.056
F0029  11-28-2008  20:48:12.781  97.3   10.4   2.071
F0030  11-28-2008  20:48:14.843  97.4   10.2   2.076
F0031  11-28-2008  20:48:16.906  97.1   10.2   2.063
F0032  11-28-2008  20:48:18.953  97.0   10.1   2.053
RPM    2.08      CC [sec] ANTENNA REPETITION TIME
CC      ***** STOP FRAMEDATA SECTION *****

```

Figure 6. Ship speed recorded during the radar data collection process.

Bell et al., proposed a method for georeferencing radar data by correcting ship heading errors using high-resolution GPS and heading data, synchronized with the ship's network. Lund et al. [49,50] expanded this approach by applying georeferencing to each radar pulse individually, accounting for ship motion and heading variations. Gangeskar [25] demonstrated the effectiveness of real-time motion compensation using vessel motion data (e.g., GPS, gyroscope) to ensure accurate radar-derived surface current estimates, even in moving installations. Together, these methods greatly enhance radar accuracy in dynamic environments.

Building on these methods, the starting position, ship speed, and heading for each radar image sequence are used in our approach. Each radar pixel is mapped to a geographic reference frame, from which sub-image sequences are extracted to enhance the accuracy of motion compensation during surface current estimation.

Figure 7 shows the effect of motion compensation. In Figure 7a, the sub-region is extracted from the radar image before motion compensation, where distortions are visible due to vessel movement. In contrast, Figure 7b presents the same sub-region after applying motion compensation, showing a clearer and more stable region. The compensation process corrects the distortions caused by the ship's movement, providing more accurate data for further analysis.

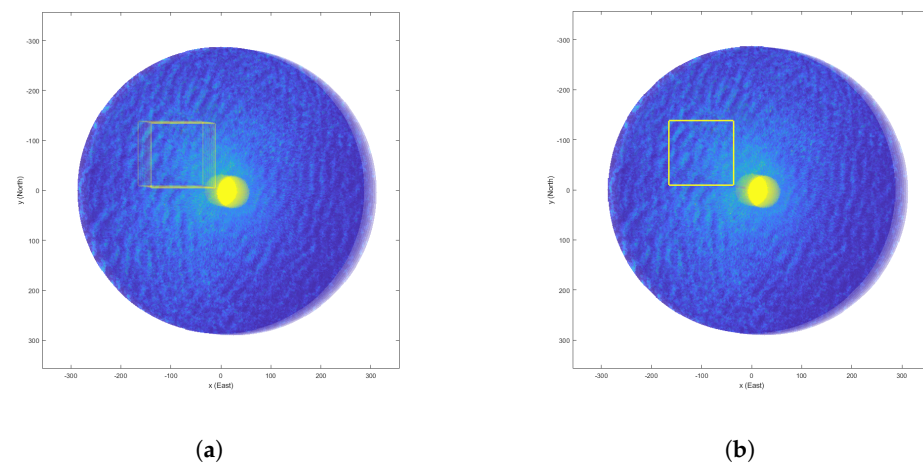


Figure 7. (a) The extracted sub-region (framed in yellow square) before motion compensation. (b) The extracted sub-region (framed in yellow square) after motion compensation.

(d) Surface Current Estimation Analysis

After applying motion compensation to eliminate the effects of ship movement, the surface current was directly extracted from the motion-compensated radar imagery. Figure 8a shows the comparison of surface current speed, and Figure 8b displays the comparison of surface current direction. The results are based on sub-regions of the radar image that have been motion-compensated, ensuring that errors caused by ship movement have been minimized. In Figure 8a, the improved PCS method closely follows the true values, with fewer fluctuations and deviations, especially in regions where the surface current speed changes rapidly, while the original PCS method and NSP method exhibit larger discrepancies. Similarly, in Figure 8b, the improved PCS method delivers a more precise estimation of surface current direction, particularly in regions with sharp directional changes. The original PCS and NSP methods, even after motion compensation, struggle to maintain the same level of accuracy in these areas.

Figure 9a,c,e show the distribution of the differences in the east (x) and north (y) components of the current vector obtained by WaMos and the improved PCS, PCS, and NSP methods. The colour intensity of each scatter point represents the corresponding WaMos-measured surface current speed. Moreover, Figure 9b,d,f present the relationship between the WaMos current directions (indicated by different colour intensities) and the error distribution for different methods. The improved PCS method exhibits minimal error dispersion. This tight clustering highlights the method's reliability across different speed conditions, with errors remaining small even at high speeds. The PCS method shows a relatively wider error spread, indicating that it may be more sensitive to variations in current speed compared to the improved PCS method. In contrast, the NSP method has the broadest error range for the data used in this study. The spread increases, particularly for high-speed conditions.

Table 3 provides the error analysis of surface current estimation based on the 2008 radar data. The improved PCS method, which includes motion compensation, achieves the highest CC in both speed (0.85) and direction (0.88), along with the lowest RMSD values for speed (0.08 m/s) and direction (26.9°). In comparison, the original PCS method exhibits slightly lower CCs and higher RMSD values.

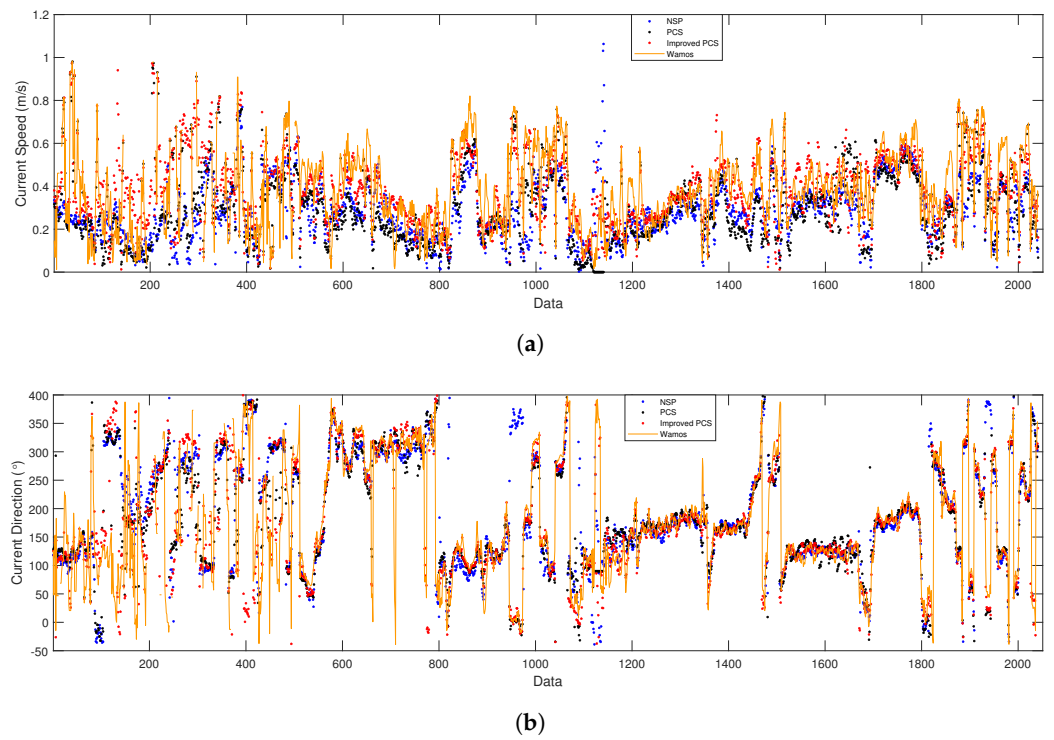


Figure 8. (a) Comparison of surface current speed and (b) surface current direction obtained from Decca radar data.

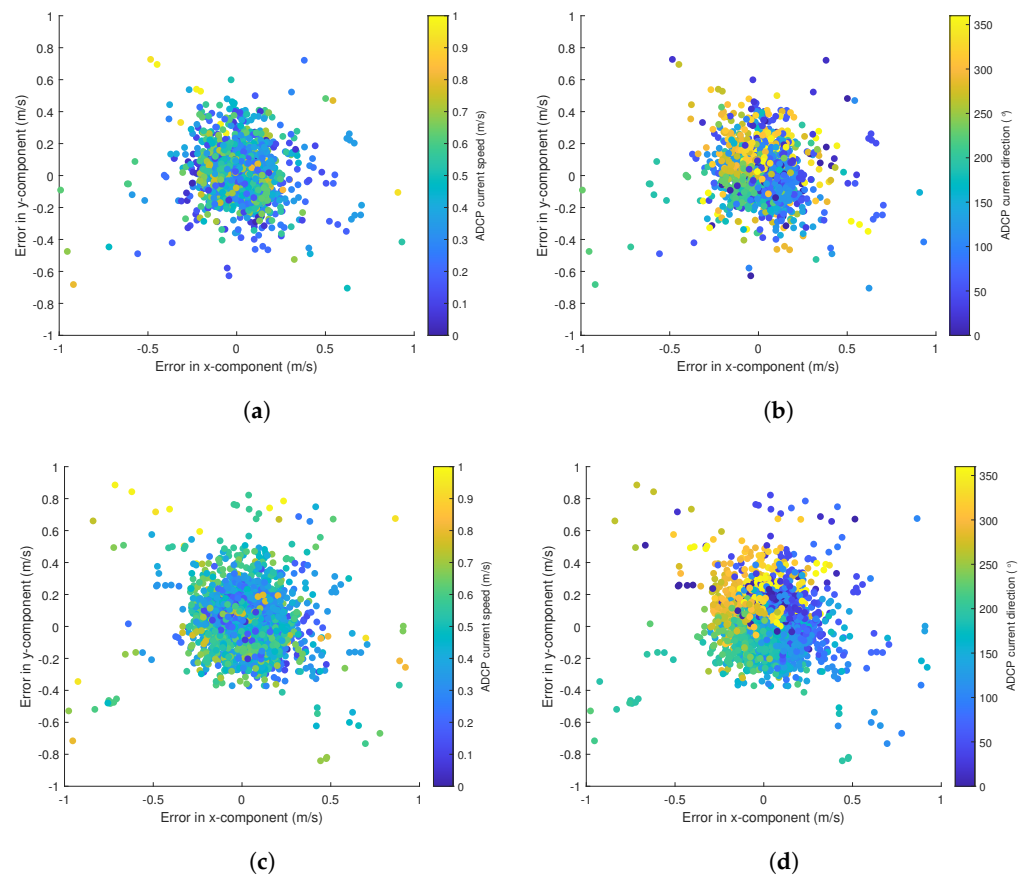


Figure 9. Cont.

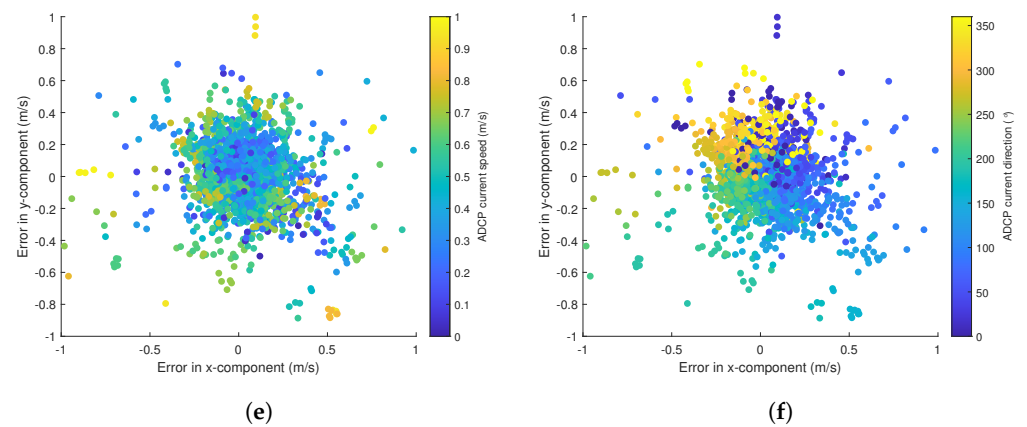


Figure 9. Scatter plot of the difference in the east (x) and north (y) components of the current vector measured by WaMos and the radar along with the corresponding surface current speed using the (a) improved PCS, (c) PCS, and (e) NSP methods, along with the corresponding surface current direction using the (b) improved PCS, (d) PCS, and (f) NSP methods.

Table 3. Error analysis of surface current estimation based on Decca radar data.

Method	CC		RMSD	
	Speed	Direction	Speed [m/s]	Direction [°]
Improved PCS	0.85	0.88	0.08	26.9
PCS	0.79	0.81	0.14	30.7
NSP	0.74	0.76	0.18	34.3

4.2.2. Analysis of Koden Radar Data

(a) Data Description

The radar data for this study were acquired from an X-band Koden marine radar system mounted on a 106-foot mobile tower at Guadalupe Dunes, CA, USA [51]. The data were collected between 15 September and 23 October 2017. The radar system operates at a frequency of 9.45 GHz, utilizing horizontal polarization (HH) for both the transmission and reception of radar pulses. Only radar images captured during periods with wind speeds exceeding 3 m/s and moderate-to-high sea states were included in the analysis. This filtering process resulted in a dataset comprising 2713 valid radar images, which were used for surface current estimation. The reference data are the 30 s block-averaged quality-controlled ADCP data [52].

(b) Surface Current Comparison

In the analysis of the 2017 radar data, shown in Table 4 and Figure 10, the improved PCS method demonstrates superior performance in estimating surface current speed and direction compared to both the PCS and NSP methods. It should be noted that after applying a 3D FFT and subsequent energy filtering, the amount of data that remained after being converted to the PCS domain was significantly reduced. This reduction is primarily due to the relatively small variation in wave direction energy caused by the surface current motion in this dataset. One possible reason for this small variation could be the specific sea-state conditions during the data collection period, where lower wind speeds or calmer seas resulted in less pronounced wave-current interactions. As a result, the surface current-induced changes in wave direction energy were not as pronounced as in other datasets, leading to fewer effective data points in the PCS domain. Due to this limitation, the overall accuracy of the surface current estimations from this dataset was lower compared to the Decca radar data. Data points with poor quality, where the PCS algorithm fails to estimate results, are excluded from the error analysis. As illustrated in Figure 10a, the retrieved current speed using the improved PCS method closely aligns with

the ADCP data, particularly in regions where the current undergoes significant dynamic changes. The RMSD for the improved PCS method is 0.09 m/s, which is slightly lower than for the PCS (0.11 m/s) and NSP (0.12 m/s) methods, as shown in Table 4. Similarly, the surface current direction estimates shown in Figure 10b reflect the improved PCS method's better performance. The RMSD for current direction is reduced to 30.1° for the improved PCS method, compared to 34.7° for PCS and 35.1° for NSP. The scatter plots shown in Figure 11 provide a visual comparison of the retrieved current speed and direction against the reference ADCP data for three different methods: improved PCS, PCS, and NSP. In Figure 11a,b, the improved PCS method demonstrates a high degree of correlation between the retrieved current speed and direction and the ADCP reference values, as evidenced by the close clustering of data points along the 1:1 line. This suggests that the improved algorithm yields more accurate results in both speed and direction estimations.

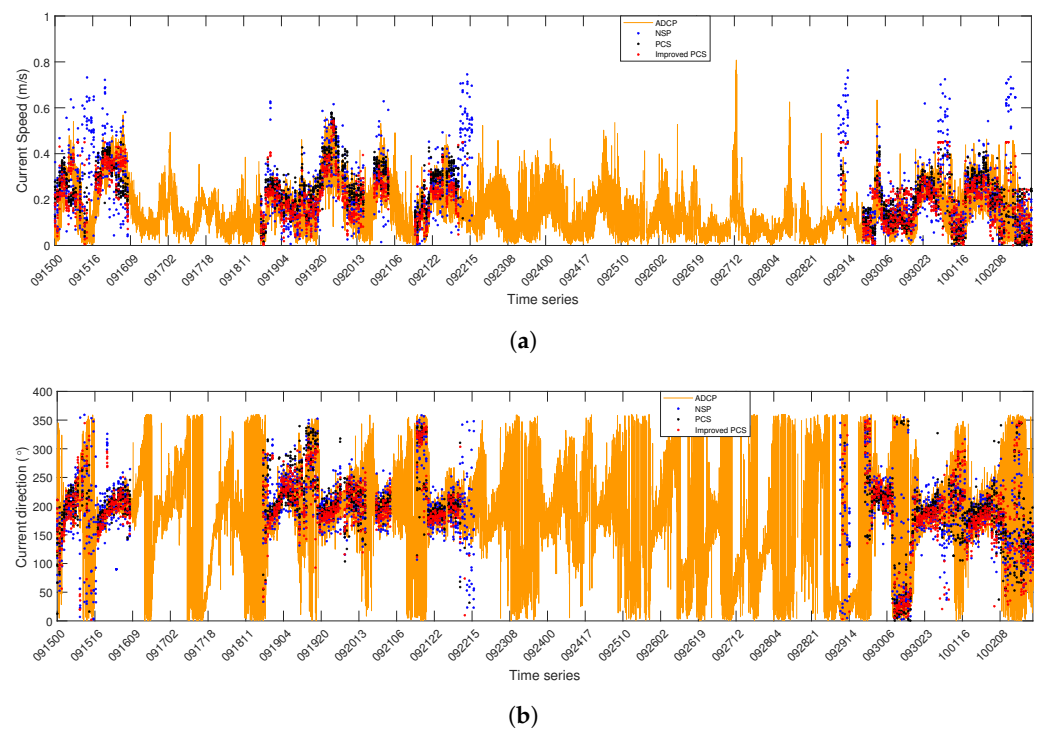


Figure 10. (a) Comparison of surface current speed and (b) surface current direction obtained from Koden radar data.

Table 4. Error analysis of surface current estimation based on Koden radar data.

Method	CC		RMSD		Bias	
	Speed	Direction	Speed [m/s]	Direction [°]	Speed [m/s]	Direction [°]
Improved PCS	0.75	0.82	0.09	30.1	0.01	−2.8
PCS	0.72	0.77	0.11	34.7	0.04	−3.9
NSP	0.70	0.73	0.12	35.1	0.06	−4.3

For the PCS method, shown in Figure 11c,d, a larger spread of points is observed, particularly in the current direction plot (d), indicating greater discrepancies between the retrieved values and the ADCP reference values, which implies lower accuracy compared to the improved PCS method.

In the NSP method's results, illustrated in Figure 11e,f, an even wider spread is noticeable, especially in the plot (f) for the current direction, where data points are significantly scattered, further highlighting the poorer performance of this method in accurately estimating the current direction when compared to both PCS and improved PCS.

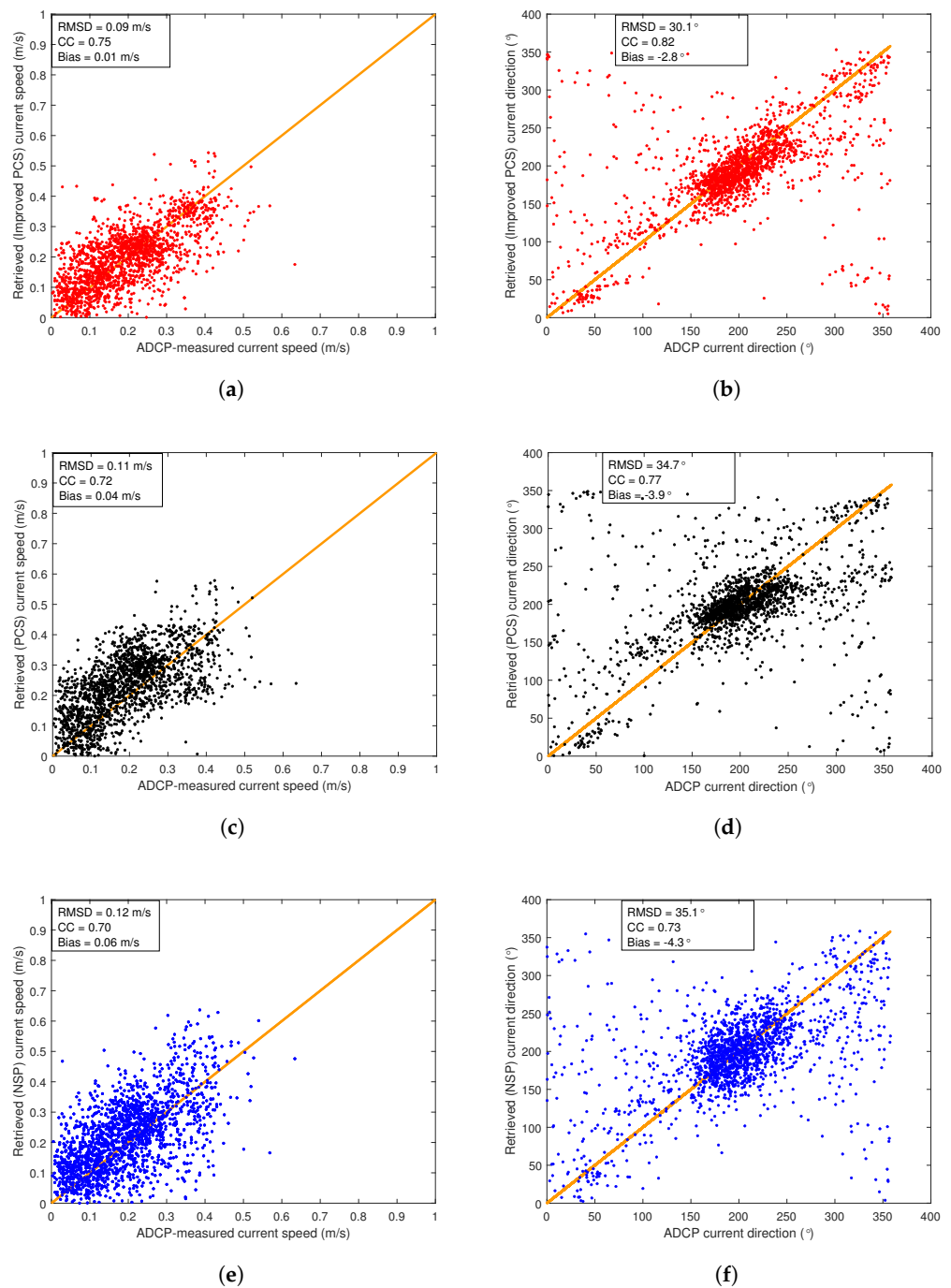


Figure 11. (a) Scatter plot comparing ADCP current speed to the retrieved current speed using the improved PCS method. (b) Scatter plot comparing ADCP current direction to the retrieved current direction using the improved PCS method. (c) Scatter plot comparing ADCP current speed to the retrieved current speed using the PCS method. (d) Scatter plot comparing ADCP current direction to the retrieved current direction using the PCS method. (e) Scatter plot comparing ADCP current speed to the retrieved current speed using the NSP method. (f) Scatter plot comparing ADCP current direction to the retrieved current direction using the NSP method.

In addition, the scatter plot of the differences in the east (x) and north (y) components of the current vector obtained by ADCP and the radar are presented in Figure 12, along with the ADCP-derived surface current speed and direction. The improved PCS method shows errors that are closest to zero in both the x and y components. The original PCS method

has a broader error range, especially along the x-axis. In contrast, the NSP method has the largest error scope. Overall, it can be observed that the improved PCS is the most accurate.

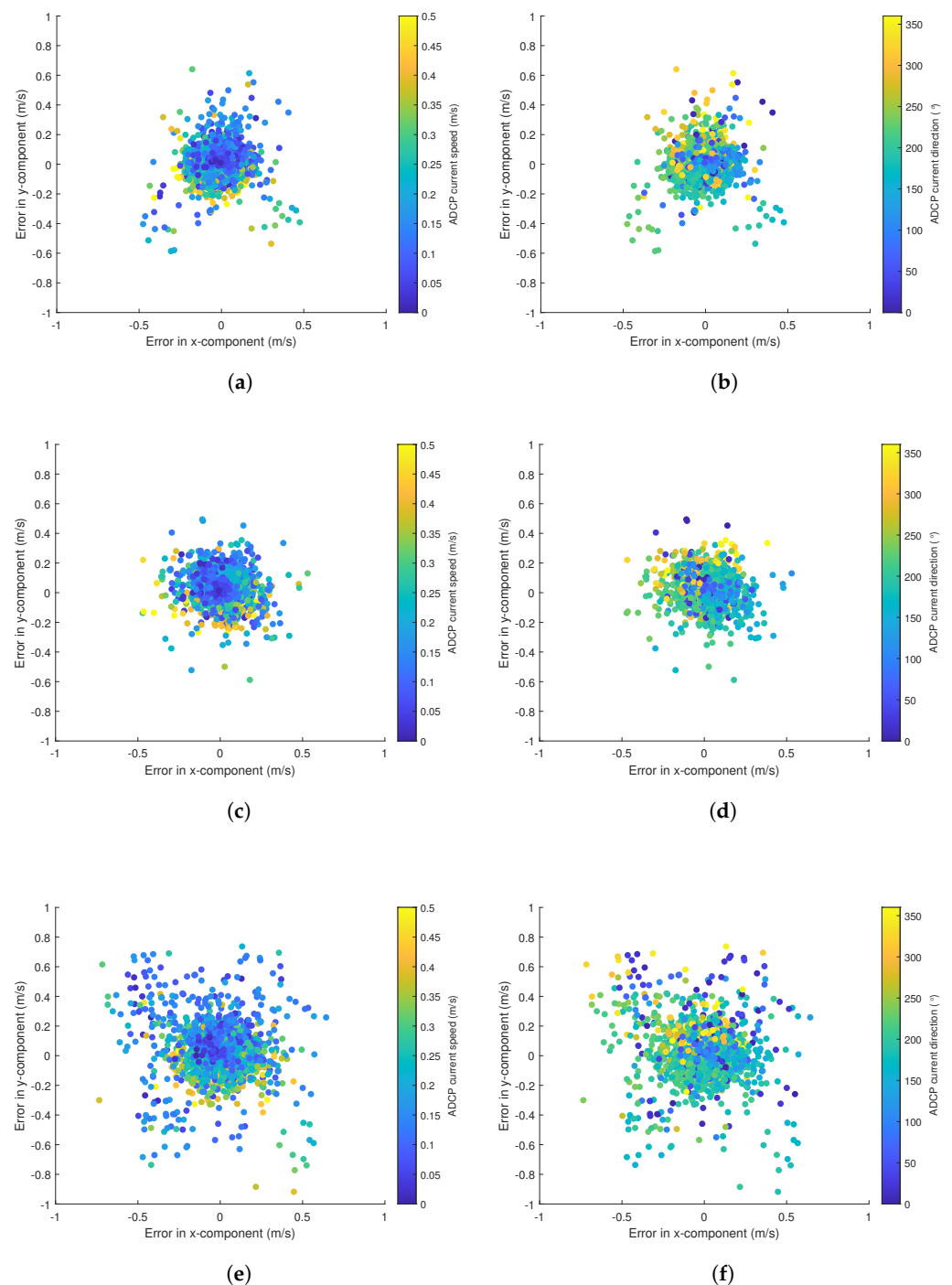


Figure 12. Scatter plot of the difference in the east (x) and north (y) components of the current vector measured by ADCP and the radar along with the corresponding surface current speed using the (a) improved PCS, (c) PCS, and (e) NSP methods, as well as the corresponding surface current direction using the (b) improved PCS, (d) PCS, and (f) NSP methods.

This analysis underscores the higher accuracy of the improved PCS method in estimating both current speed and direction, as reflected by the tighter clustering of points around the ADCP reference line. Even for a dataset with lower overall precision, the improved PCS method consistently maintains the highest level of accuracy compared to other methods.

5. Discussion

The analysis of the simulated data reveals that the improved PCS algorithm significantly enhances the accuracy of surface current retrieval, particularly at lower rotation speeds (RPM = 24). This improvement highlights the effectiveness of extracting reliable data points from the overall dataset, minimizing the influence of errors caused by curve fitting for individual wavenumber vectors. The substantial improvement in accuracy for the Decca radar dataset, which operates at 24 RPM, further demonstrates the algorithm's practical effectiveness in real-world scenarios. The increased precision achieved with the Decca data provides strong evidence of the improved PCS method's success in addressing the limitations of the original approach.

While the difference between the improved and original PCS algorithms is less pronounced at higher rotation speeds (RPM = 48) in the simulated data, the Koden radar dataset (also RPM = 48) still shows slight improvements with the improved PCS method. The presence of noise and other real-world factors in the Koden data allows the improved PCS algorithm to demonstrate the value of its individual steps, even in cases where the overall dataset quality is low. The ability of the improved PCS method to maintain accuracy in these conditions highlights its robustness against environmental noise and other data inconsistencies that affect current estimation.

As previously noted, the initial PCS data from the Koden radar dataset are relatively sparse, resulting in lower overall accuracy compared to the Decca radar data. This underscores a key area for future improvement: enhancing the algorithm's ability to maintain high precision in current extraction when the dispersion shell contains fewer data points. The challenge lies not only in removing noise interference but also in preserving the extraction accuracy even when the available data are limited. Addressing this limitation will be crucial for further advancing the PCS algorithm's performance in real-world applications with less-than-ideal data conditions.

According to [2,53], wind-driven Ekman flows strongly influence currents within the top 10 m, and the current gradually changes direction and its speed decreases as depth increases. Thus, the ADCP current direction and speed depend on the depth of measurements. X-band radars provide an estimation of current close to the surface. Unfortunately, ADCP data for the top 10 m were unavailable. As a result, only the ADCP data at a depth of 11.2 m were utilized for comparison in this experiment, although the ADCP data from depths ranging from 10 m to 150 m were analyzed. A depth of 11.2 m was chosen since the data at such a depth showed the closest alignment with the radar-derived results. The difference between the radar-derived current and ADCP sub-surface data can be partially attributed to the difference in the depths of their measurement.

6. Conclusions

This paper presents an improved PCS algorithm for retrieving surface currents from X-band marine radar images. The improvements address several limitations of the original PCS method, particularly in the presence of noise, aliasing, and data outliers. By introducing filtering techniques and leveraging directional symmetry for noise reduction, the improved PCS method provides more accurate and reliable current estimates.

The results from the simulated radar data demonstrate that the improved PCS method consistently outperforms both the original PCS and NSP methods. The tests performed under different radar RPMs also prove the robustness of the improved method, which was less sensitive to aliasing effects compared to the original PCS.

In real data applications, both the Decca radar data and the Koden radar data further validated the improved PCS algorithm. The comparison with ADCP reference data confirmed that the improved method achieved a higher CC and lower RMSD than the original method. Specifically, the improved PCS method has a speed CC of 0.85 and an RMSD of 0.08 m/s for the Decca data and a 15% reduction in the RMSD and a 12% improvement in the CC compared to the original PCS methods for the data collected by the Koden radar, which are better results than for the original PCS and NSP methods.

In conclusion, the improved PCS method represents an advancement over traditional methods. It is more robust in real-world applications, where environmental noise and data anomalies are more common. This method may experience reduced effectiveness when the data quality is poor or when there is a lack of significantly concentrated wave energy. In such cases, the algorithm's ability to accurately retrieve ocean currents can be diminished, as it relies heavily on the presence of strong and coherent wave signatures to filter noise and perform accurate estimations. However, even under these conditions, its accuracy remains superior to other methods. Nevertheless, it is crucial to develop improved algorithms to better mitigate these limitations and further enhance performance in such challenging scenarios. Further improvements might focus on handling low-quality data and testing the robustness of the proposed method under varying sea states.

Author Contributions: Conceptualization, Y.L.; software, writing—original draft preparation, Y.L.; writing—review, editing, and revision, Z.Y. and W.H. All authors have read and agreed to the published version of the manuscript.

Funding: The work of Weimin Huang was supported by the Natural Sciences and Engineering Research Council of Canada Discovery Grants under Grant NSERC RGPIN-2024-04442.

Data Availability Statement: The original contributions presented in the study are included in the article, further inquiries can be directed to the corresponding author.

Acknowledgments: The authors would like to express gratitude to E. Thornhill from Defence Research and Development Canada (DRDC), along with Merrick C. Haller and R. Pittman from Oregon State University, for their provision of the radar and anemometer data.

Conflicts of Interest: The authors declare that there are no conflicts of interest.

References

1. Röhrs, J.; Sutherland, G.; Jeans, G.; Bedington, M.; Sperrevik, A.K.; Dagestad, K.F.; Gusdal, Y.; Mauritzen, C.; Dale, A.; LaCasce, J.H. Surface currents in operational oceanography: Key applications, mechanisms, and methods. *J. Oper. Oceanogr.* **2023**, *16*, 60–88. [[CrossRef](#)]
2. Lund, B.; Graber, H.C.; Tamura, H.; Collins, C.O., III; Varlamov, S.M. A new technique for the retrieval of near-surface vertical current shear from marine X-band radar images. *J. Geophys. Res. Oceans* **2015**, *120*, 8466–8486. [[CrossRef](#)]
3. Blockley, E.W.; Martin, M.J.; Hyder, P. Validation of FOAM near-surface ocean current forecasts using Lagrangian drifting buoys. *Ocean Sci.* **2012**, *8*, 551–565. [[CrossRef](#)]
4. Krauss, W.; Dengg, J.; Hinrichsen, H. The response of drifting buoys to currents and wind. *J. Geophys. Res.* **1989**, *94*, 3201–3210. [[CrossRef](#)]
5. Lane, A.; Knight, P.; Player, R. Current measurement technology for near-shore waters. *Coast. Eng.* **1999**, *37*, 343–368. [[CrossRef](#)]
6. Bourgerie, R.; Garner, T.; Shih, H. Coastal current measurements using an ADCP in a streamlined sub-surface mooring buoy. In Proceedings of the OCEANS '02 MTS/IEEE, Biloxi, MI, USA, 29–31 October 2002; Volume 2, pp. 736–741. [[CrossRef](#)]
7. Weller, R.A.; Davis, R.E. A vector measuring current meter. *Deep-Sea Res. I Oceanogr. Res. Pap.* **1980**, *27*, 565–581. [[CrossRef](#)]
8. Lucas, N.; Simpson, J.; Rippeth, T.; Old, C. Measuring turbulent dissipation using a tethered ADCP. *J. Atmos. Ocean. Technol.* **2014**, *31*, 1826–1837. [[CrossRef](#)]
9. Young, I.R.; Rosenthal, W.; Ziemer, F. A three-dimensional analysis of marine radar images for the determination of ocean wave directionality and surface currents. *J. Geophys. Res.-Oceans* **1985**, *90*, 1049–1059. [[CrossRef](#)]
10. Barrick, D.E.; Evans, M.W.; Weber, B.L. Ocean surface currents mapped by radar. *Science* **1977**, *198*, 138–144. [[CrossRef](#)] [[PubMed](#)]
11. Essen, H.H.; Gurgel, K.W.; Schlick, T. On the accuracy of current measurements by means of HF radar. *IEEE J. Ocean. Eng.* **2000**, *25*, 472–480. [[CrossRef](#)]
12. Hickey, K.; Khan, R.; Walsh, J. Parametric estimation of ocean surface currents with HF radar. *IEEE J. Ocean. Eng.* **1995**, *20*, 139–144. [[CrossRef](#)]
13. Wang, W.; Gill, E.W.; Huang, W. Comparison of spectral estimation methods for rapidly varying currents obtained by high-frequency radar. *IEEE J. Ocean. Eng.* **2017**, *42*, 556–565. [[CrossRef](#)]
14. Serafino, F.; Lugni, C.; Soldovieri, F. A novel strategy for the surface current determination from marine X-band radar data. *IEEE Geosci. Remote Sens. Lett.* **2010**, *7*, 231–235. [[CrossRef](#)]
15. Quilfen, Y.; Chapron, B. Ocean surface wave-current signatures from satellite altimeter measurements. *Geophys. Res. Lett.* **2019**, *46*, 253–261. [[CrossRef](#)]
16. Shemer, L.; Marom, M.; Markman, D. Estimates of currents in the nearshore ocean region using interferometric Synthetic Aperture Radar. *J. Geophys. Res. Oceans* **1993**, *98*, 7001–7010. [[CrossRef](#)]

17. Huang, W.; Liu, X.; Gill, E.W. Ocean wind and wave measurements using X-band marine radar: A comprehensive review. *Remote Sens.* **2017**, *9*, 1261. [\[CrossRef\]](#)
18. Novi, L.; Raffa, F.; Serafino, F. Comparison of measured surface currents from high frequency (HF) and X-band radar in a marine protected coastal area of the Ligurian sea: Toward an integrated monitoring system. *Remote Sens.* **2020**, *12*, 3074. [\[CrossRef\]](#)
19. Izquierdo, P.; Guedes Soares, C. Analysis of sea waves and wind from X-band radar. *Ocean Eng.* **2005**, *32*, 1404–1419. [\[CrossRef\]](#)
20. Liu, X.; Huang, W.; Gill, E.W. Wind direction estimation from rain-contaminated marine radar data using the ensemble empirical mode decomposition method. *IEEE Trans. Geosci. Remote Sens.* **2017**, *55*, 1833–1841. [\[CrossRef\]](#)
21. Yang, Z.; Huang, W. SWHFormer: A Vision Transformer for significant wave height estimation from nautical radar images. *IEEE Trans. Geosci. Remote Sens.* **2024**, *62*, 5104213. [\[CrossRef\]](#)
22. Nieto-Borge, J.C.; Hessner, K.; Jarabo-Amores, P. Signal-to-noise ratio analysis to estimate ocean wave heights from X-band marine radar image time series. *IET Radar Sonar Navig.* **2008**, *2*, 35–41. [\[CrossRef\]](#)
23. Chen, X.; Huang, W. Spatial-temporal convolutional gated recurrent unit network for significant wave height estimation from shipborne marine radar data. *IEEE Trans. Geosci. Remote Sens.* **2022**, *60*, 4201711. [\[CrossRef\]](#)
24. Yang, Z.; Huang, W. Wave height estimation from X-band radar data using variational mode decomposition. *IEEE Geosci. Remote Sens. Lett.* **2022**, *19*, 1505405. [\[CrossRef\]](#)
25. Gangeskar, R. Verifying high-accuracy ocean surface current measurements by X-Band radar for fixed and moving installations. *IEEE Trans. Geosci. Remote Sens.* **2018**, *56*, 4845–4855. [\[CrossRef\]](#)
26. Senet, C.; Seemann, J.; Ziemer, F. The near-surface current velocity determined from image sequences of the sea surface. *IEEE Trans. Geosci. Remote Sens.* **2001**, *39*, 492–505. [\[CrossRef\]](#)
27. Gangeskar, R. Ocean current estimated from X-band radar sea surface, images. *IEEE Trans. Geosci. Remote Sens.* **2002**, *40*, 783–792. [\[CrossRef\]](#)
28. Senet, C.M.; Seemann, J.; Flampouris, S.; Ziemer, F. Determination of bathymetric and current maps by the method DiSC based on the analysis of nautical X-band radar image sequences of the sea surface (November 2007). *IEEE Trans. Geosci. Remote Sens.* **2008**, *46*, 2267–2279. [\[CrossRef\]](#)
29. Shen, C.; Huang, W.; Gill, E.W.; Carrasco, R.; Horstmann, J. An algorithm for surface current retrieval from X-band marine radar images. *Remote Sens.* **2015**, *7*, 7753–7767. [\[CrossRef\]](#)
30. Huang, W.; Gill, E. Surface current measurement under low sea state using dual polarized X-band nautical radar. *IEEE J. Sel. Top. Appl. Earth Obs. Remote Sens.* **2012**, *5*, 1868–1873. [\[CrossRef\]](#)
31. Chen, Z.; Zhang, B.; Kudryavtsev, V.; He, Y.; Chu, X. Estimation of sea surface current from X-band marine radar images by cross-spectrum analysis. *Remote Sens.* **2019**, *11*, 1031. [\[CrossRef\]](#)
32. Wu, L.C.; Doong, D.J.; Lai, J.W. Sea surface current estimation from a semi-enclosed bay using coastal X-band radar images. *IEEE Trans. Geosci. Remote Sens.* **2024**, *62*, 4210511. [\[CrossRef\]](#)
33. Wang, S.; Rheem, C.K. Research on optimal machine learning algorithm for sea surface observation using X-band Doppler radar. In Proceedings of the OCEANS 2023-Limerick, Limerick, Ireland, 5–8 June 2023; pp. 1–6.
34. Hessner, K.G.; El Naggar, S.; von Appen, W.J.; Strass, V.H. On the reliability of surface current measurements by X-band marine radar. *Remote Sens.* **2019**, *11*, 1030. [\[CrossRef\]](#)
35. Derkani, M.H.; Alberello, A.; Nelli, F.; Bennetts, L.G.; Hessner, K.G.; MacHutchon, K.; Reichert, K.; Aouf, L.; Khan, S.; Toffoli, A. Wind, waves, and surface currents in the Southern Ocean: Observations from the Antarctic Circumnavigation Expedition. *Earth Syst. Sci. Data.* **2021**, *13*, 1189–1209. [\[CrossRef\]](#)
36. Huang, W.; Carrasco, R.; Shen, C.; Gill, E.W.; Horstmann, J. Surface current measurements using X-band marine radar with vertical polarization. *IEEE Trans. Geosci. Remote Sens.* **2016**, *54*, 2988–2997. [\[CrossRef\]](#)
37. Huang, W.; Gill, E.; An, J. Iterative least-squares-based wave measurement using X-band nautical radar. *IET Radar Sonar Navig.* **2014**, *8*, 853–863. [\[CrossRef\]](#)
38. Nieto-Borge, J.C.; Rodríguez, G.R.; Hessner, K.; González, P.I. Inversion of Marine Radar Images for Surface Wave Analysis. *J. Atmos. Ocean. Technol.* **2004**, *21*, 1291–1300. [\[CrossRef\]](#)
39. Grubbs, F.E. Procedures for detecting outlying observations in samples. *Technometrics* **1969**, *11*, 1–21. [\[CrossRef\]](#)
40. Sain, S.R. Multivariate locally adaptive density estimation. *Comput. Stat. Data Anal.* **2002**, *39*, 165–186. [\[CrossRef\]](#)
41. Silverman, B.W. *Density Estimation for Statistics and Data Estimation*; Chapman and Hall: London, UK, 1986.
42. Wan, X.; Wang, W.; Liu, J.; Tong, T. Estimating the sample mean and standard deviation from the sample size, median, range and/or interquartile range. *BMC Med. Res. Methodol.* **2014**, *14*, 135. [\[CrossRef\]](#)
43. Li, Y.; Huang, W. An algorithm for ocean current inversion from X-band marine radar images. In Proceedings of the 2024 IEEE International Geoscience and Remote Sensing Symposium (IGARSS), Athens, Greece, 7–12 July 2024; pp. 5956–5960. [\[CrossRef\]](#)
44. Nomiya, D.H.; Hirayama, T. Evaluation of marine radar as an ocean-wave-field detector through full numerical simulation. *J. Mar. Sci. Technol.* **2003**, *8*, 88–98. [\[CrossRef\]](#)
45. Huang, W.; Gill, E. Simulation analysis of sea surface current extraction from microwave nautical radar images. In Proceedings of the 2012 19th IEEE International Conference on Image Processing, Orlando, FL, USA, 30 September–3 October 2012; pp. 2673–2676.
46. Ewing, J.A.; Laing, A.K. Directional spectra of seas near full development. *J. Phys. Oceanogr.* **1987**, *17*, 1696–1706. [\[CrossRef\]](#)
47. Serafino, F.; Lugni, C.; Nieto Borge, J.C.; Zamparelli, V.; Soldovieri, F. Bathymetry determination via X-band radar data: A new strategy and numerical results. *Sensors* **2010**, *10*, 6522–6534. [\[CrossRef\]](#) [\[PubMed\]](#)

48. Bell, P.; Osler, J. Mapping bathymetry using X-band marine radar data recorded from a moving vessel. *Ocean Dyn.* **2011**, *61*, 2141–2156. [[CrossRef](#)]
49. Lund, B.; Collins, C., III; Graber, H.; Terrill, E. On the imaging of surface gravity waves by marine radar: Implications for a moving platform. In Proceedings of the 13th International Workshop on Wave Hindcasting and Forecasting & 4th Coastal Hazard Symposium, Banff, AB, Canada, 27 October–1 November 2013.
50. Lund, B.; Graber, H.C.; Hessner, K.; Williams, N.J. On shipboard marine X-band radar near-surface current “calibration”. *J. Atmos. Ocean. Technol.* **2015**, *32*, 1928–1944. [[CrossRef](#)]
51. Haller, M.C.; Honegger, D.A.; Pittman, R.; O’Dea, A.; Simpson, A. Real-time marine radar observations of nearshore waves and flow structures from shore-based towers. In Proceedings of the 2019 IEEE/OES Twelfth Current, Waves and Turbulence Measurement (CWTM), San Diego, CA, USA, 10–13 March 2019; pp. 1–7.
52. Lerczak, J.A.; Barth, J.A.; Calantoni, J.; Colosi, J.A.; MacKinnon, J.A.; Moum, J.N.; Waterhouse, A.F.; Thomson, J.; McSweeney, J.M.; Becherer, J.; et al. Offshore moorings: Moorings deployed in 10–150 m water depth on the inner- to mid-shelf. In *Observations and Model Simulations from the Inner-Shelf Dynamics Experiment (ISDE)*; UC San Diego Library Digital Collections: La Jolla, CA, USA, 2022. [[CrossRef](#)]
53. Ekman, V.W. On the influence of the Earth’s rotation on ocean currents. *Ark. Mat. Astron. Fys.* **1905**, *2*, 1–53.

Disclaimer/Publisher’s Note: The statements, opinions and data contained in all publications are solely those of the individual author(s) and contributor(s) and not of MDPI and/or the editor(s). MDPI and/or the editor(s) disclaim responsibility for any injury to people or property resulting from any ideas, methods, instructions or products referred to in the content.